Supplementary Information for

Solving matrix equations in one step with crosspoint resistive arrays

Zhong Sun, Giacomo Pedretti, Elia Ambrosi, Alessandro Bricalli, Wei Wang and Daniele Ielmini

Daniele Ielmini
Email: daniele.ielmini@polimi.it

This PDF file includes:

> Supplementary text
> Figs. S1 to S23
> Tables S1
> References for SI reference citations

Methods

Experimental devices. The RRAM devices in this work use a thin (5 nm) HfO_2 film as a switching layer, deposited by e-beam evaporation on a confined graphitic carbon bottom electrode (BE). Without breaking the vacuum during evaporation, a thin layer of Ti was deposited as top electrode (TE) on top of the HfO_2 dielectric layer. The deposited Ti layer has been reported to act as an oxygen scavenger (1), leading to the formation of an oxygen-exchange layer of TiO_x between Ti and HfO_2. The oxygen-exchange layer is instrumental in increasing the local oxygen-vacancies concentration in HfO_2, which enhances the leakage current in the pristine state. As consequences, the forming voltage of the devices is reduced, and a unidirectional switching behavior is forced, where set and reset transitions take place under positive and negative voltages applied to the TE, respectively. The forming process was operated in DC regime by applying a voltage sweep from 0 to 5 V, with the voltage applied to the TE and the BE being grounded. The forming process induces a soft breakdown of dielectric HfO_2 layer, which initiated the CF formation and the resistive switching behavior. The DC conduction and switching characteristics of the RRAM were collected by a Keysight B1500A Semiconductor Parameter Analyzer, which was connected to the experimental device in a conventional probe station for electrical characterization.

Experimental measurements. For all the experiments, the devices were arranged in the crosspoint configuration on a custom Printed Circuit Board (PCB, Fig. S1), and an Agilent B2902A Precision Source/Measure Unit was employed to program the devices to different conductance states. Matrix-vector multiplication (MVM) and matrix inversion experiments were carried out on a custom PCB with operational amplifiers (OAs) of model AD823 (Analog Devices). For eigenvectors experiments, Voltage Limiting Amplifiers of model OPA698 (Texas Instruments) were used to limit the maximum voltage across the RRAM devices, protecting the devices from electrical damages. RRAM devices were connected with the BE to the amplifiers' inverting-input nodes and with the TE to the amplifiers' output terminals. A BAS40-04 diode is connected between every amplifier output and ground, to limit the voltages within ± 0.7 V, avoiding conductance changes of RRAM devices. All the input signals were given by a 4-channels arbitrary waveform generator (Aim-TTi TGA12104) and applied to fixed input resistances, which were connected between the input and the amplifiers' inverting-input nodes. The amplifiers' output voltages were monitored by an oscilloscope (LeCroy Wavesurfer 3024). The board was powered by a BK Precision 1761 DC power supply. The board for matrix-inversion circuit experiments of a single positive matrix (a crosspoint array of resistive switches or discrete resistors) is shown in Fig. S1.
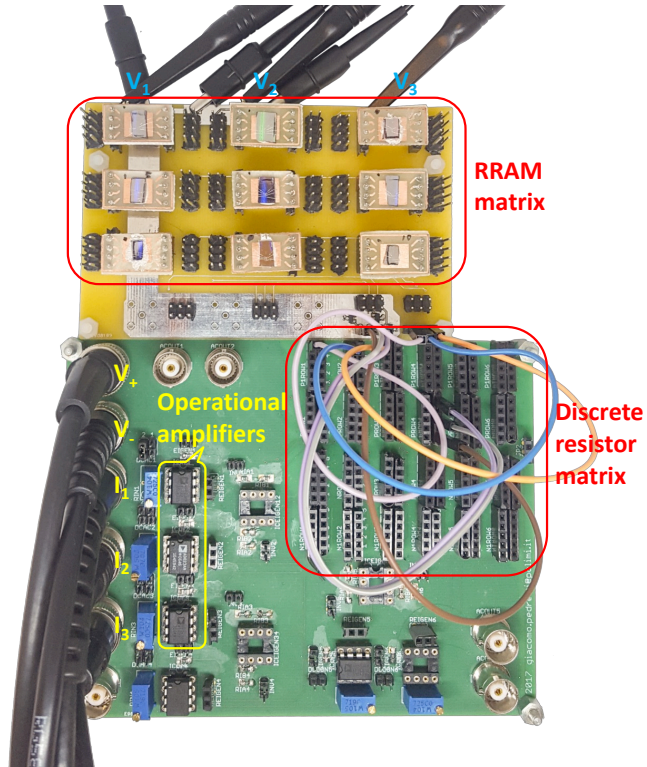
Fig. S1. The board for matrix-inversion circuit experiments of a single positive matrix. V_+ and V_- are supply voltages for OAs, I_1, I_2 and I_3 are input currents, and V_1, V_2 and V_3 are output voltages. The discrete resistors were used to stabilize the feedback circuit when mounting the RRAM devices, and they were removed after the RRAM matrix was completed. For experiments of mixed matrices, another board was added.
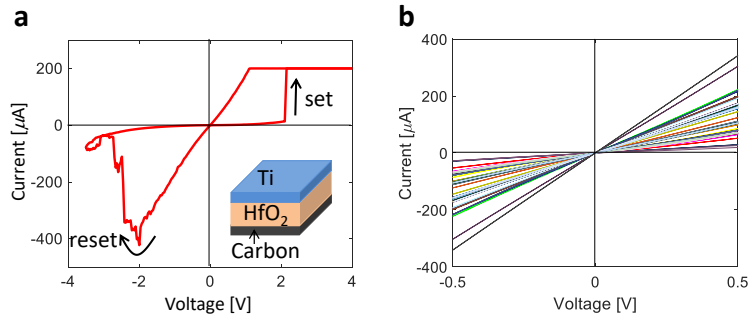
Fig. S2. Current-voltage (*I-V*) characteristics of the resistive switching device. (a) Measured *I-V* characteristics of the device showing change of the conductance. The inset shows the structure of the resistive switching device employed in this work. In this case, I_C is 200 μA, and V_{stop} is -3.5 V. (b) Measured *I-V* characteristics of the resistive switching device with multilevel low resistance state (LRS). To avoid conduction non-linearity of resistive switches, the devices were programmed to the LRS, with a conductance of few hundreds of μS.
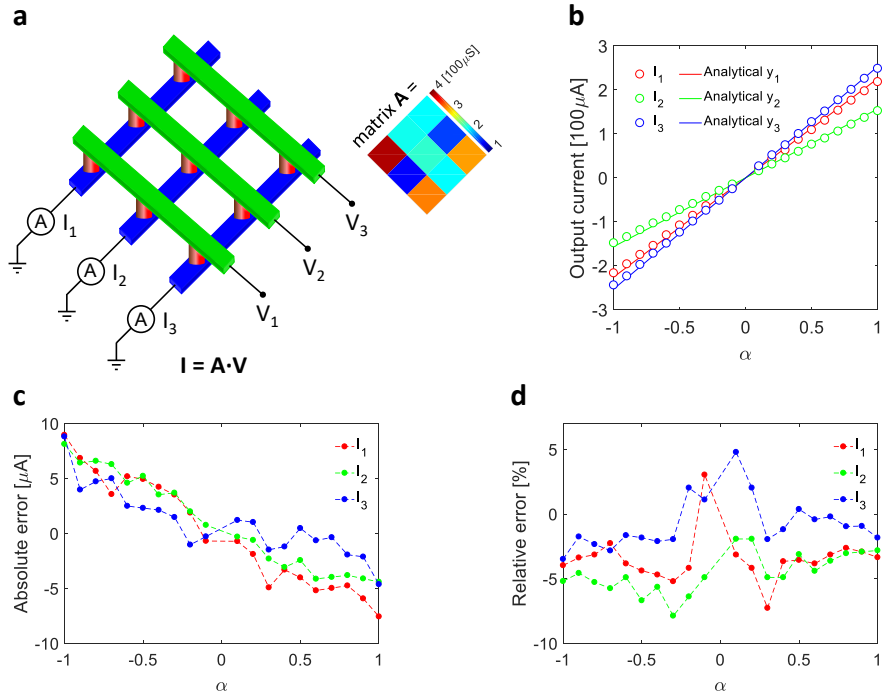
Fig. S3. Matrix-vector multiplication (MVM) in a crosspoint resistive array. (a) Crosspoint array for MVM and a concerned square matrix A. The conductance matrix is the same one in Fig. 1A in the main text. To perform MVM, a voltage vector $V = [V_1; V_2; V_3]$ is applied to the columns, and a current vector $I = [I_1; I_2; V_3]$ is collected at the rows. (b) Experimental results of the MVM, consisting of the measured current at array rows as a function of the parameter α controlling the amplitude of the input voltage. The latter was $V = \alpha \cdot [0.2; 0.3; 0.4]$ V, and α was changed uniformly in the range from -1 to 1. The experimental currents are compared with the analytical results showing good accuracy. (c) Absolute errors of the MVM. (d) Relative errors of the MVM.

Table S1. Summary of numerical matrices utilized in experiment in this work. The transformation units for conductance and output voltage, the condition numbers (κ) of adopted matrices for solving linear systems are also included.

Matrices		Transformation unit	Positions	κ
	$A = \begin{bmatrix} 3.85 & 2.17 & 2.09 \\ 1.36 & 2.23 & 1.56 \\ 3.23 & 2.08 & 3.15 \end{bmatrix}$	100 μS	**Fig. 1a**	9.2526
	$A^{-1} = \begin{bmatrix} 0.547 & -0.308 & -0.218 \\ 0.13 & 0.706 & -0.416 \\ -0.623 & -0.118 & 0.796 \end{bmatrix}$	1 V	**Fig. 1e**	
$B = \begin{bmatrix} 4.33 & 2.88 & 1.51 \\ 0.95 & 3.40 & 3.85 \\ 3.94 & 1.13 & 3.24 \end{bmatrix}$	$C = \begin{bmatrix} 1.97 & 0.83 & 5.05 \\ 4.57 & 0.83 & 3.30 \\ 1.97 & 3.70 & 1.33 \end{bmatrix}$	100 μS	**Fig. 2b**	
	$A = \begin{bmatrix} 2.36 & 2.05 & -3.54 \\ -3.62 & 2.57 & 0.55 \\ 1.97 & -2.57 & 1.91 \end{bmatrix}$		**Fig. 2b**	9.5074
	$A^{-1} = \begin{bmatrix} 0.396 & 0.314 & 0.618 \\ 0.51 & 0.706 & 0.703 \\ 0.278 & 0.624 & 0.83 \end{bmatrix}$	1 V	**Fig. 2c**	
	$A^{-1} = \begin{bmatrix} 1.94 & 1.45 & 3.22 \\ 2.42 & 3.35 & 3.39 \\ 1.27 & 3.12 & 4.21 \end{bmatrix}$	500 μS	**Fig. 2d**	8.5803
	$\left(A^{-1}\right)^{-1} = \begin{bmatrix} 2.11 & 2.21 & -3.42 \\ -3.26 & 2.35 & 0.76 \\ 1.83 & -2.36 & 1.75 \end{bmatrix}$	1 V	**Fig. 2e**	

Continue in the next page.

| Matrices		Transformation unit	Positions	κ
$B = \begin{bmatrix} 5.24 & 2.91 & 1.8 \\ 3.39 & 3.25 & 3.43 \\ 3.15 & 1.16 & 7.58 \end{bmatrix}$	$C = \begin{bmatrix} 3.30 & 3.71 & 3.29 \\ 4.98 & 1.33 & 3.26 \\ 4.57 & 1.33 & 4.98 \end{bmatrix}$	100 μS	**Fig. S13a**	
	$A = \begin{bmatrix} 1.94 & -0.80 & -1.49 \\ -1.59 & 1.92 & 0.17 \\ -1.42 & -0.17 & 2.60 \end{bmatrix}$		**Fig. S13a**	16.9235
	$A^{-1} = \begin{bmatrix} 2.272 & 1.072 & 1.472 \\ 1.9 & 1.44 & 1.216 \\ 1.12 & 0.496 & 1.168 \end{bmatrix}$	1 V	**Fig. S13b**	
	$A^{-1} = \begin{bmatrix} 2.17 & 1.04 & 1.43 \\ 1.92 & 1.46 & 1.23 \\ 1.16 & 0.5 & 1.17 \end{bmatrix}$	100 μS	**Fig. S13c**	19.2496
	$\left(A^{-1}\right)^{-1} = \begin{bmatrix} 1.952 & -0.864 & -1.6 \\ -1.44 & 1.664 & 0.064 \\ -1.472 & 0.32 & 2.56 \end{bmatrix}$	1 V	**Fig. S13d**	
	$A = \begin{bmatrix} 3.57 & 4.01 & 7.80 \\ 2.45 & 3.48 & 1.61 \\ 3.34 & 1.51 & 0.57 \end{bmatrix}$	100 μS	**Fig. 3a**	
	$A = \begin{bmatrix} 0 & 0 & 1.00 & 0.47 \\ 0.31 & 0 & 0 & 0 \\ 0.31 & 0.49 & 0 & 0.51 \\ 0.31 & 0.49 & 0 & 0 \end{bmatrix}$	684 μS	**Fig. 3d**	
	$A = \begin{bmatrix} 2.11 & 1.00 & 0.30 & 0.55 & 2.79 \\ 1.00 & 4.56 & 1.33 & 0.55 & 2.12 \\ 0.67 & 0.37 & 0.67 & 0.67 & 0.37 \\ 0.30 & 0.55 & 0.37 & 2.78 & 0.55 \\ 0.37 & 1.34 & 0.67 & 0.55 & 1.33 \end{bmatrix}$	10 μS	**Fig. S7a**	15.7641
	$A^{-1} = \begin{bmatrix} 0.375 & 0.275 & 0.703 & -0.018 & -1.398 \\ -0.017 & 0.398 & -0.278 & 0.103 & -0.563 \\ -0.431 & -0.317 & 1.351 & -0.415 & 1.19 \\ -0.005 & -0.003 & -0.091 & 0.409 & -0.126 \\ 0.129 & -0.318 & -0.561 & -0.06 & 1.159 \end{bmatrix}$	1 V	**Fig. S7c**	
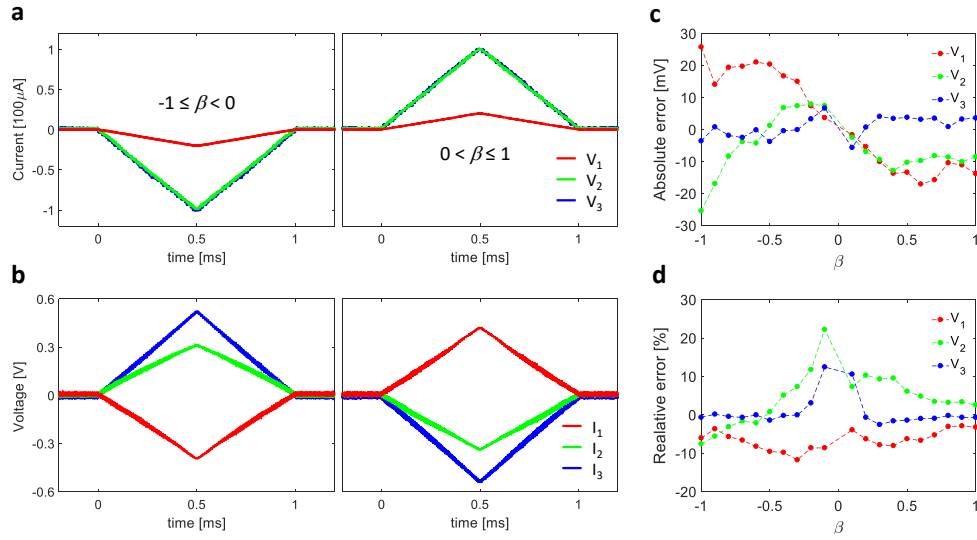
Fig. S4. Solutions of systems of linear equations. (a) Oscilloscope traces of the input current, representing the known term *b* in *Ax = b*, where the relative current amplitude *β* covered both positive and negative values. The input currents were generated by independent voltage sources with triangular waveforms with output resistance R_s = 10 kΩ connected to the inverting-input nodes of the OAs. (b) Output voltage measured at the columns of the crosspoint array. (c) Absolute errors of the linear system solutions. (d) Relative errors of the linear system solutions.
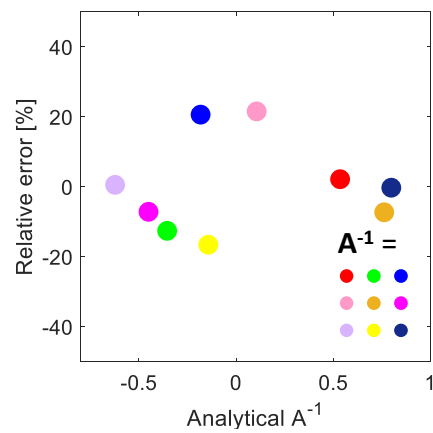
Fig. S5. Relative errors of the matrix inversion in Fig. 1*E*. Relative error is defined as $\Delta M_{ij}/M_{ij}$, where ΔM_{ij} is the difference between the measured matrix coefficient and the ideal one M_{ij}.

9

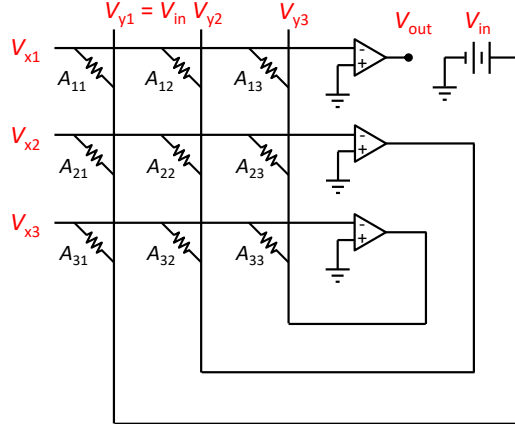**Loop gains of the feedback circuit for solving linear systems.**

Fig. S6. Calculation of the loop gain G_{loop} for the matrix-inversion circuit. The crosspoint circuit of Fig. 1 in the main text is cut at the first output for evaluating the loop gain G_{loop1}, obtained by forcing an input signal V_{in} and measuring the corresponding output V_{out} at the other end of the loop, where $G_{loop1} = V_{out}/V_{in}$. This is obtained by solving Kirchhoff's law and Ohm's law for the circuit, resulting in the following six equations:

$$\left(V_{y1} - V_{x1}\right)A_{11} + \left(V_{y2} - V_{x1}\right)A_{12} + \left(V_{y3} - V_{x1}\right)A_{13} = 0, \; V_{out} = -G_{OL}V_{x1},$$

$$\left(V_{y1} - V_{x2}\right)A_{21} + \left(V_{y2} - V_{x2}\right)A_{22} + \left(V_{y3} - V_{x2}\right)A_{23} = 0, \; V_{y2} = -G_{OL}V_{x2},$$

$$\left(V_{y1} - V_{x3}\right)A_{31} + \left(V_{y2} - V_{x3}\right)A_{32} + \left(V_{y3} - V_{x3}\right)A_{33} = 0, \; V_{y3} = -G_{OL}V_{x3},$$

which result in the loop gain of the first loop (G_{loop1}),

$$G_{loop1} = \frac{V_{out}}{V_{in}} = -\frac{G_{OL}}{A_1^*} \frac{\begin{vmatrix} A_{11} & A_{12} & A_{13} \\ A_{21} & A_{22} + \dfrac{A_2^*}{G_{OL}} & A_{23} \\ A_{31} & A_{32} & A_{33} + \dfrac{A_3^*}{G_{OL}} \end{vmatrix}}{\begin{vmatrix} A_{22} + \dfrac{A_2^*}{G_{OL}} & A_{23} \\ A_{32} & A_{33} + \dfrac{A_3^*}{G_{OL}} \end{vmatrix}}$$

where $A_1^* = A_{11} + A_{12} + A_{13}$, $A_2^* = A_{21} + A_{22} + A_{23}$, $A_3^* = A_{31} + A_{32} + A_{33}$ and G_{OL} is the open-loop gain of amplifiers, which is infinite for ideal amplifiers, and was assumed equal to 2×10^5 in the simulations. Since G_{OL} is very large, the additional terms in diagonal elements can be ignored, leading to:

$$G_{loop1} = -\frac{G_{OL}}{A_1^*} \frac{\begin{vmatrix} A_{11} & A_{12} & A_{13} \\ A_{21} & A_{22} & A_{23} \\ A_{31} & A_{32} & A_{33} \end{vmatrix}}{\begin{vmatrix} A_{22} & A_{23} \\ A_{32} & A_{33} \end{vmatrix}} = -\frac{G_{OL}}{A_1^*} \frac{1}{\left(A^{-1}\right)_{11}},$$

where $(A^{-1})_{11}$ is the first diagonal element of A^{-1}. The similar calculation of the gains of the second and third loops yields:

$$G_{loop2} = -\frac{G_{OL}}{A_2^*} \frac{1}{\left(A^{-1}\right)_{22}}$$

$$G_{loop3} = -\frac{G_{OL}}{A_3^*} \frac{1}{\left(A^{-1}\right)_{33}}$$

where $(A^{-1})_{22}$ and $(A^{-1})_{33}$ are the second and third diagonal elements of A^{-1}, respectively.

As a result, G_{loop} has the opposite sign as the diagonal elements of A^{-1}. We conclude that, for G_{loop} to be negative thus ensuring virtual ground at the crosspoint rows, the diagonal elements in A^{-1} must be positive. Also, this analysis indicates that G_{loop} is inversely proportional to the diagonal elements of A^{-1}.
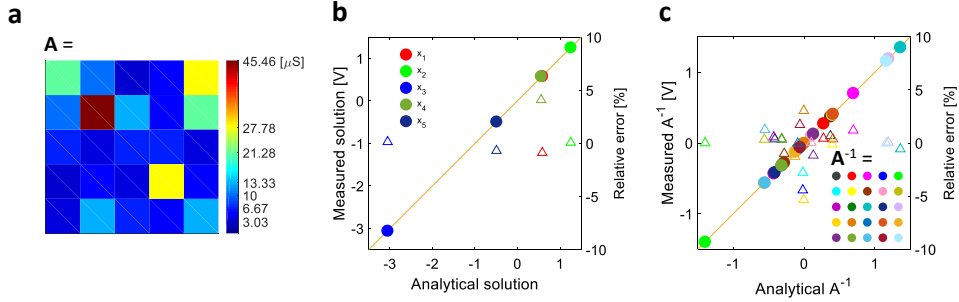
Fig. S7. Solution of a linear system and matrix inversion for a 5×5 matrix. (a) Conductance values
A of the 5×5 crosspoint array, mapping the coefficient matrix. The 5×5 crosspoint array was
implemented with discrete resistors. The transformation units between the real-valued
matrices/vectors and the physical implementations were $G_0 = 10 \mu S$, $I_0 = 10 \mu A$ and $V_0 = 1$ V for
resistors' conductance, input current and output voltage, respectively. (b) Experimental solution of the
linear system $Ax = b$, with input-current vector $I = -b = -[0.5; 1.5; -1; 1; -0.5]I_0$. The experimental
solution is compared with the analytical solution. The triangles are calculated relative errors, which
are plotted as the right *y*-axis. (c) Experimental matrix inversion of *A*, showing high accuracy
compared to the analytical inversion thanks to high precision and linearity of discrete resistors. The
triangles are calculated relative errors, which are plotted as the right *y*-axis. It is shown that the
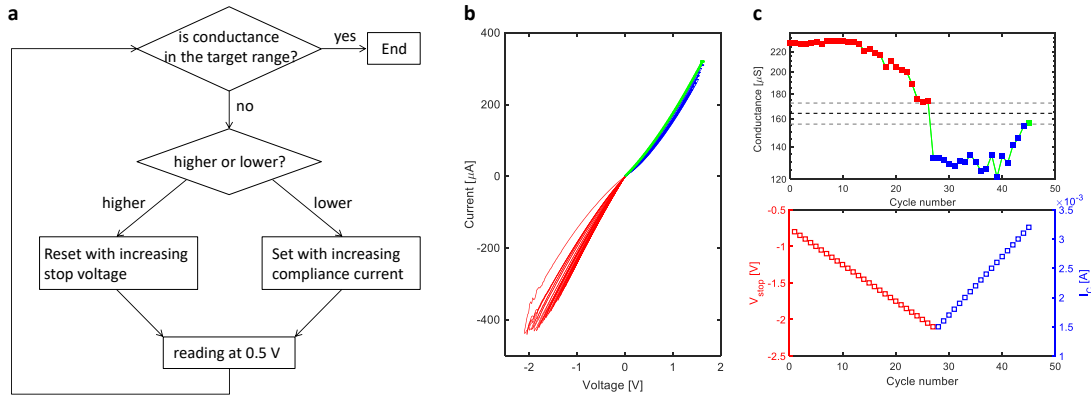relative errors are within 1% for elements not close to zero.

Fig. S8. The program-and-verify algorithm. (a) Flow diagram of the program-and-verify algorithm. For a nominal conductance value, a target range is defined with the allowed maximum error $\varepsilon = 5\%$. To achieve a value within the target range, multiple programming steps of set/reset and reading operations are carried out until the conductance falls into the target range. A set/reset operation is executed by a positive/negative voltage sweep. For instance, to reach a conductance from a higher value, incremental reset steps are conducted, consisting of negative voltage sweeps at increasing voltage. If a reset step results in a value which is lower by more than the error ε, a sequence of incremental set operations (positive voltage sweeps at increasing compliance current I_C) is executed, until the desired conductance is reached within an accuracy margin ε. (b) *I-V* curves for programming a device, indicating incremental set steps and incremental reset steps. The nominal conductance was 164 μS. (c) Readout conductance values during the program-and-verify process (top panel), the incremental stop-voltage during the reset phase and the incremental compliance current during the set phase (bottom panel). After 45 operations, the device conductance falls into the target range.
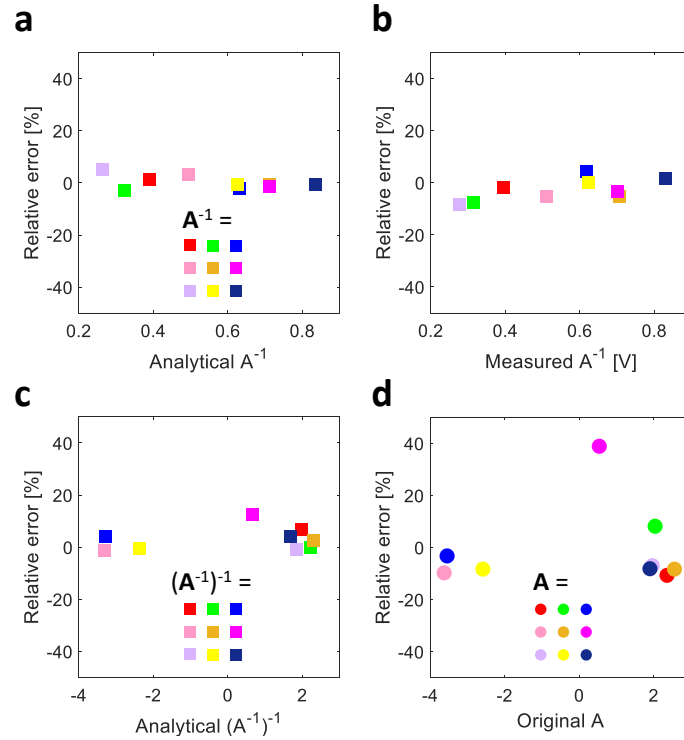
13

Fig. S9. Relative errors of the double inversion experiment in Fig. 2. (a) Relative errors of the first inversion process, *i.e.*, the measured A^{-1}. (b) Relative errors of the device programming process. (c) Relative errors of the second inversion process, *i.e.*, the measured $(A^{-1})^{-1}$. (d) The overall relative errors of the double inversion experiment.

Solving a 1-dimensional steady-state Fourier equation.

a

c

b

matrix **A**   conductance   conductance
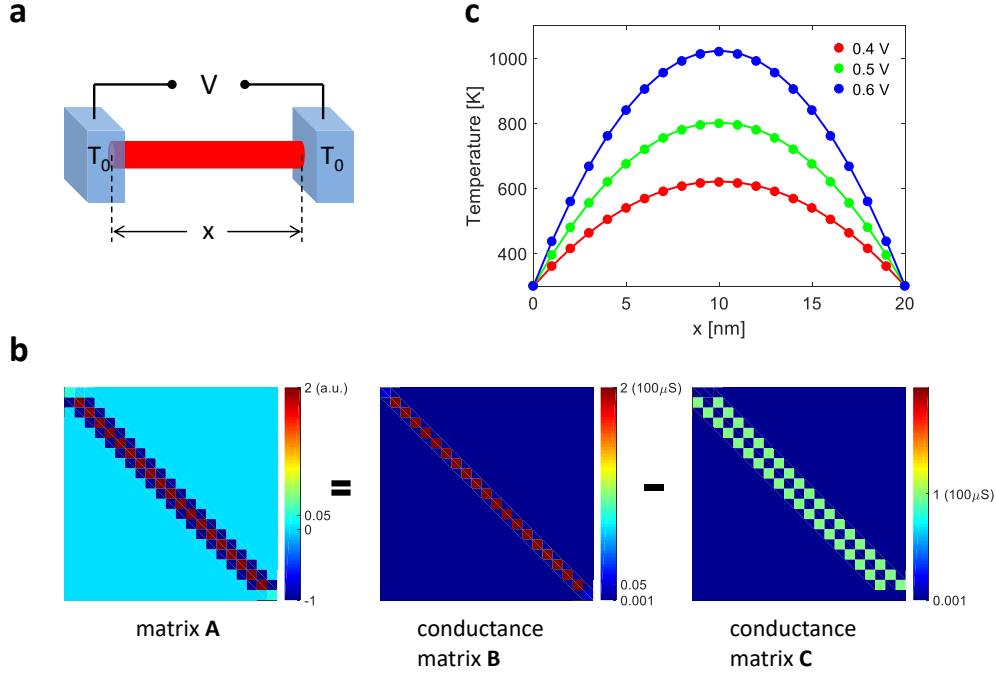   matrix **B**   matrix **C**

Fig. S10. Circuit solution of a steady-state Fourier equation. (a) 1-dimensional system for the solution of the steady-state heat equation, *e.g.*, to describe Joule heating in the filamentary path of RRAM (2, 3). A voltage V is applied across the filament, while the two extremes are kept at temperature $T_0 = 300$ K. (b) Matrix A of the coefficients obtained by discretizing the Fourier equation, and the two positive matrices B and C splitting matrix A, for the simulation case of $V = 0.6$ V. The condition number of matrix A is 304. For cases of $V = 0.4$ V and $V = 0.5$ V, the condition number of matrix A is 617 and 410, respectively. (c) Resulting temperature profile along the filament obtained by circuit simulation and from an analytical solution. The solutions are shown for 3 cases with increasing applied voltage $V = 0.4$ V, 0.5 V and 0.6 V. Compared with the analytical solutions (lines), the circuit simulations (dots) show good accuracy.

The Fourier equation in 1D reads:

$$k_{th} \frac{d^2 T}{dx^2} + \frac{V^2}{\rho l^2} = 0,$$

where k_{th} is the filament thermal conductivity, ρ is the filament resistivity, and l is the filament length. In our study, we assumed $k_{th} = 23$ W/(m • K), $\rho = 270$ mW • cm, $l = 20$ nm.

The differential equation was transformed into a linear system by a standard finite difference approach, where the filament was discretized in 20 equal segments of length $\Delta x = 1$ nm. In the *i*-th segment, the Fourier equation is thus expressed as:

$$T_{i-1} - 2T_i + T_{i+1} = -\frac{V^2}{k_{th}\rho} \cdot \left(\frac{\Delta x}{l}\right)^2.$$

A system of linear equations is thus obtained and expressed in the following matrix form:

$$
\begin{bmatrix}
-\dfrac{V^2}{k_{th}\rho T_0}\left(\dfrac{\Delta x}{l}\right)^2 & 0 & 0 & 0 & \cdots & 0 & 0 \\
1 & -2 & 1 & 0 & \cdots & 0 & 0 \\
0 & 1 & -2 & 1 & \cdots & 0 & 0 \\
\vdots & \vdots & \vdots & \vdots & \cdots & \vdots & \vdots \\
0 & 0 & 0 & 0 & \cdots & 1 & 0 \\
0 & 0 & 0 & 0 & \cdots & -2 & 1 \\
0 & 0 & 0 & 0 & \cdots & 0 & -\dfrac{V^2}{k_{th}\rho T_0}\left(\dfrac{\Delta x}{l}\right)^2
\end{bmatrix}
\begin{bmatrix}
T_1 \\ T_2 \\ T_3 \\ \vdots \\ T_{N-2} \\ T_{N-1} \\ T_N
\end{bmatrix}
= -\frac{V^2}{k_{th}\rho}\left(\frac{\Delta x}{l}\right)^2
\begin{bmatrix}
1 \\ 1 \\ 1 \\ \vdots \\ 1 \\ 1 \\ 1
\end{bmatrix}.
$$

For the above matrix, the diagonal of its inverse matrix is negative, so it does not satisfy the conditions for matrix-inversion circuit, the sign is changed in the left and right hand sides thus leading to:

$$
\begin{bmatrix}
\dfrac{V^2}{k_{th}\rho T_0}\left(\dfrac{\Delta x}{l}\right)^2 & 0 & 0 & 0 & \cdots & 0 & 0 \\
-1 & 2 & -1 & 0 & \cdots & 0 & 0 \\
0 & -1 & 2 & -1 & \cdots & 0 & 0 \\
\vdots & \vdots & \vdots & \vdots & \cdots & \vdots & \vdots \\
0 & 0 & 0 & 0 & \cdots & -1 & 0 \\
0 & 0 & 0 & 0 & \cdots & 2 & -1 \\
0 & 0 & 0 & 0 & \cdots & 0 & \dfrac{V^2}{k_{th}\rho T_0}\left(\dfrac{\Delta x}{l}\right)^2
\end{bmatrix}
\begin{bmatrix}
T_1 \\ T_2 \\ T_3 \\ \vdots \\ T_{N-2} \\ T_{N-1} \\ T_N
\end{bmatrix}
= \frac{V^2}{k_{th}\rho}\left(\frac{\Delta x}{l}\right)^2
\begin{bmatrix}
1 \\ 1 \\ 1 \\ \vdots \\ 1 \\ 1 \\ 1
\end{bmatrix},
$$

where the matrix is suitable to the circuit-based inversion. In simulation, the matrix is split into two positive matrices B and C, with matrix B satisfying the condition for matrix-inversion circuit. Then, the system of equation is solved with the two-crosspoint-array circuit. For increasing applied voltages, different linear systems will be solved, and 3 cases of $V = 0.4$ V, 0.5 V, 0.6 V are simulated. In the simulation, the same input-current vector is forced for all cases, and the final temperature distributions are obtained through timing the factor $\dfrac{V^2}{k_{th}\rho}\left(\dfrac{\Delta x}{l}\right)^2$. The simulation circuit is shown in Fig. S11.
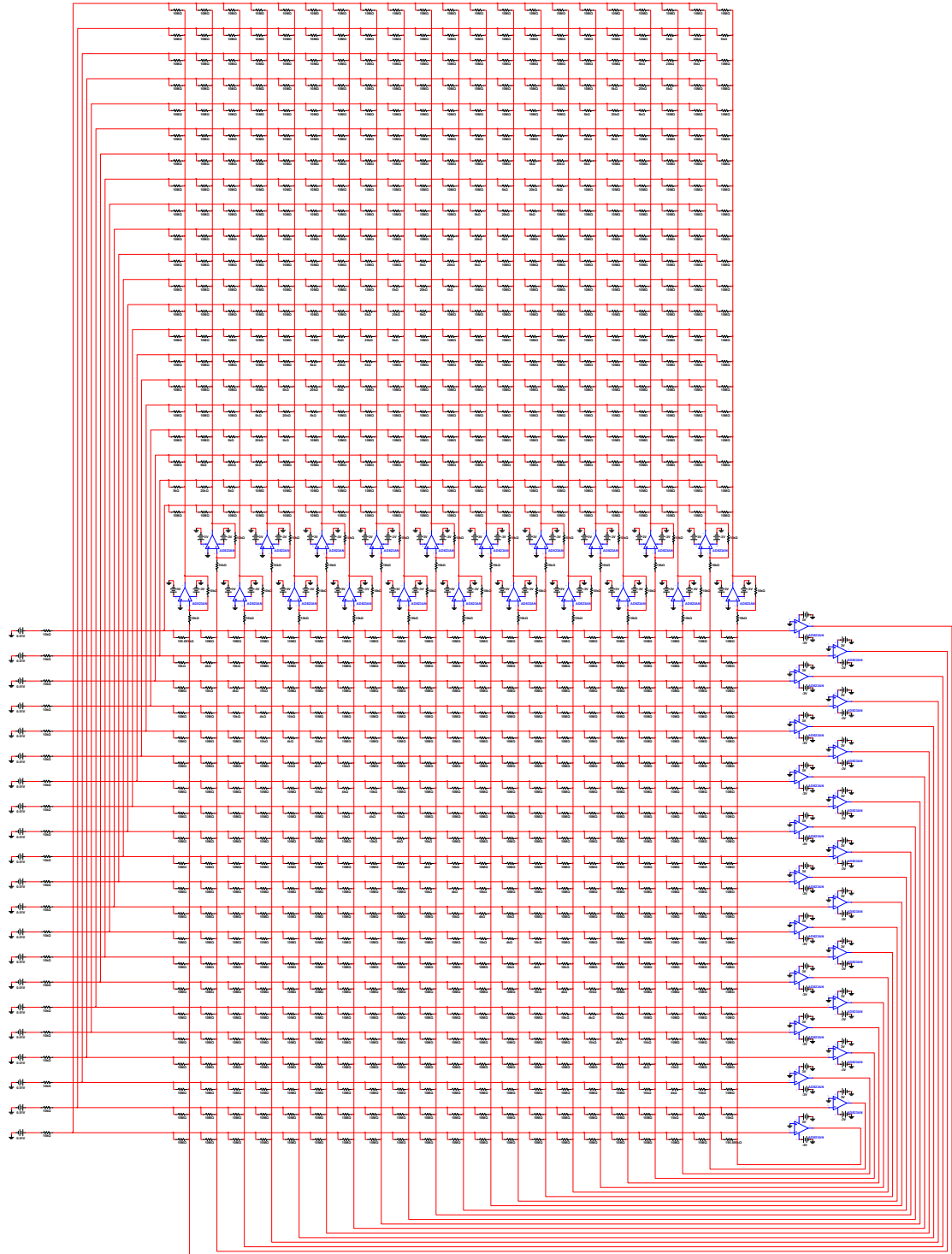
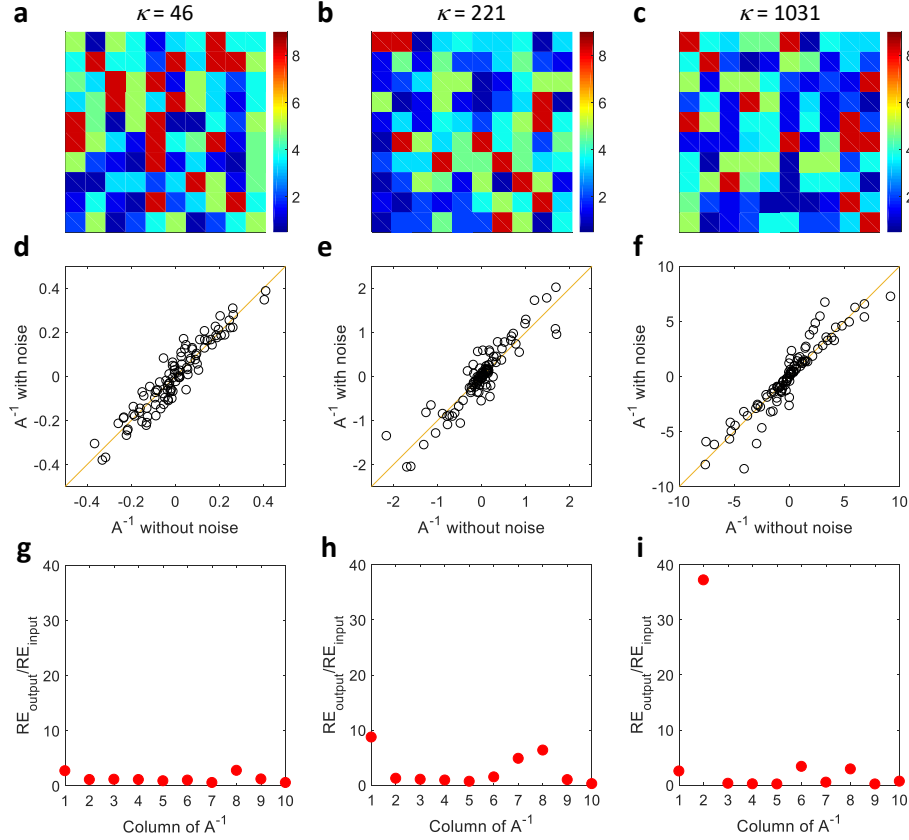**Fig. S11. Simulation circuit for solving the steady-state Fourier equation.**

Fig. S12. Condition number dependence of relative errors for solving linear systems. Three 10×10 matrices composed of random discrete values, with different condition numbers of (a) 46, (b) 221 and (c)1031. For the three matrices, their inversions were solved to study the condition number dependence of computing error, where a noise of 10% or -10% was randomly added to each element in the column vectors from the 10×10 unit matrix. (d-f) Correlation plot of the noised inverse matrix against the precise inverse for the matrix in (a-c), respectively. (g-i) Ratios of relative errors. For computing each column vector in the inverse matrix, the ratio of relative errors was calculated. The ratio of relative error of the y-axis is defined as $\frac{\|A^{-1}e\|/\|A^{-1}b\|}{\|e\|/\|b\|}$, where b is a column vector from the unit matrix, and e is a random error vector composed of ± 0.1, A^{-1} is the precise inversion of matrix A. For all cases, the relative errors of input are the same. As the condition number of matrix increases, the relative error of output increases for some columns in the inverse matrix, for instance, the 1st, 7th and 8th columns in matrix (b), the 2nd column in matrix (c), while the ones for other columns stay almost the same.
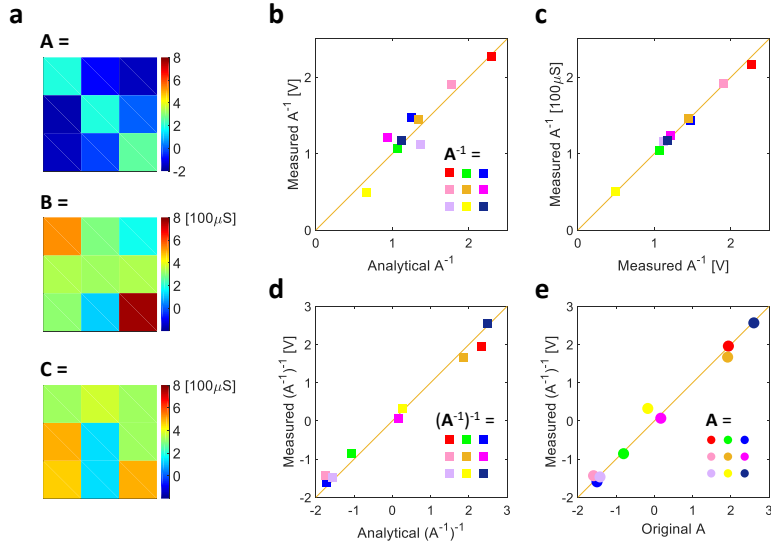
Fig. S13. Another double inversion experiment for a matrix with a larger condition number. (a) Measured values of the matrices *A*, *B*, and *C*, with *A* = *B* - *C*. In the experiment, matrix *B* was implemented by a crosspoint array of RRAM, while matrix *C* was implemented by a crosspoint array of discrete resistors. (b) Measured values of the inverse matrix A^{-1} as a function of the analytically calculated elements of A^{-1}. (c) Conductance values for matrix A^{-1} implemented in RRAM elements, as a function of the experimental values of A^{-1} in (b). The matrix A^{-1} was implemented with $G_0 = 100 \ \mu$S for RRAM conductance. (d) Measured elements of matrix $(A^{-1})^{-1}$ as a function of analytical calculations. (e) Measured elements of matrix $(A^{-1})^{-1}$ as a function with the original matrix *A*. The condition numbers of the conductance matrices *A* and A^{-1} are 16.9 and 19.2, respectively, compared to 9.5 and 8.6 of the case in Fig. 2.
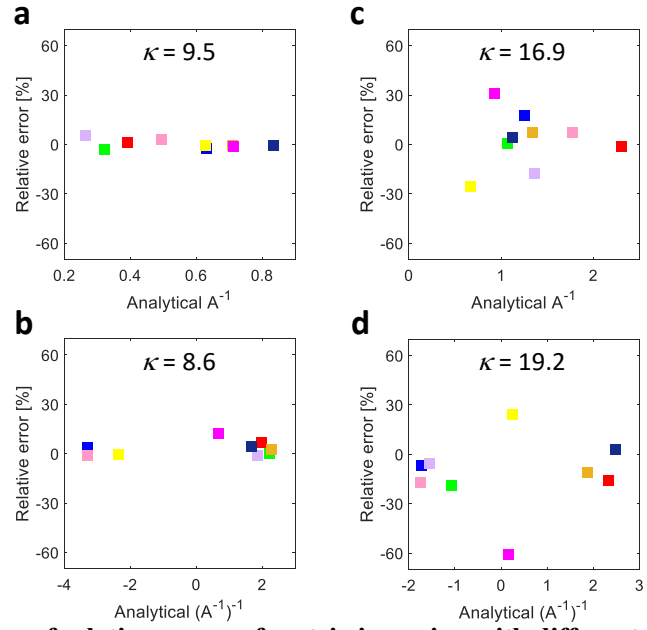
Fig. S14. Comparison of relative errors of matrix inversion with different condition numbers. (a) Relative errors of the first inversion in Fig. 2. (b) Relative errors of the second inversion in Fig. 2. (c) Relative errors of the first inversion in Fig. S13. (d) Relative errors of the second inversion in Fig. S13. The condition numbers are labeled in all plots. The double inversion experiment in Fig. S13 show larger relative errors for both processes than the one in Fig. 2.
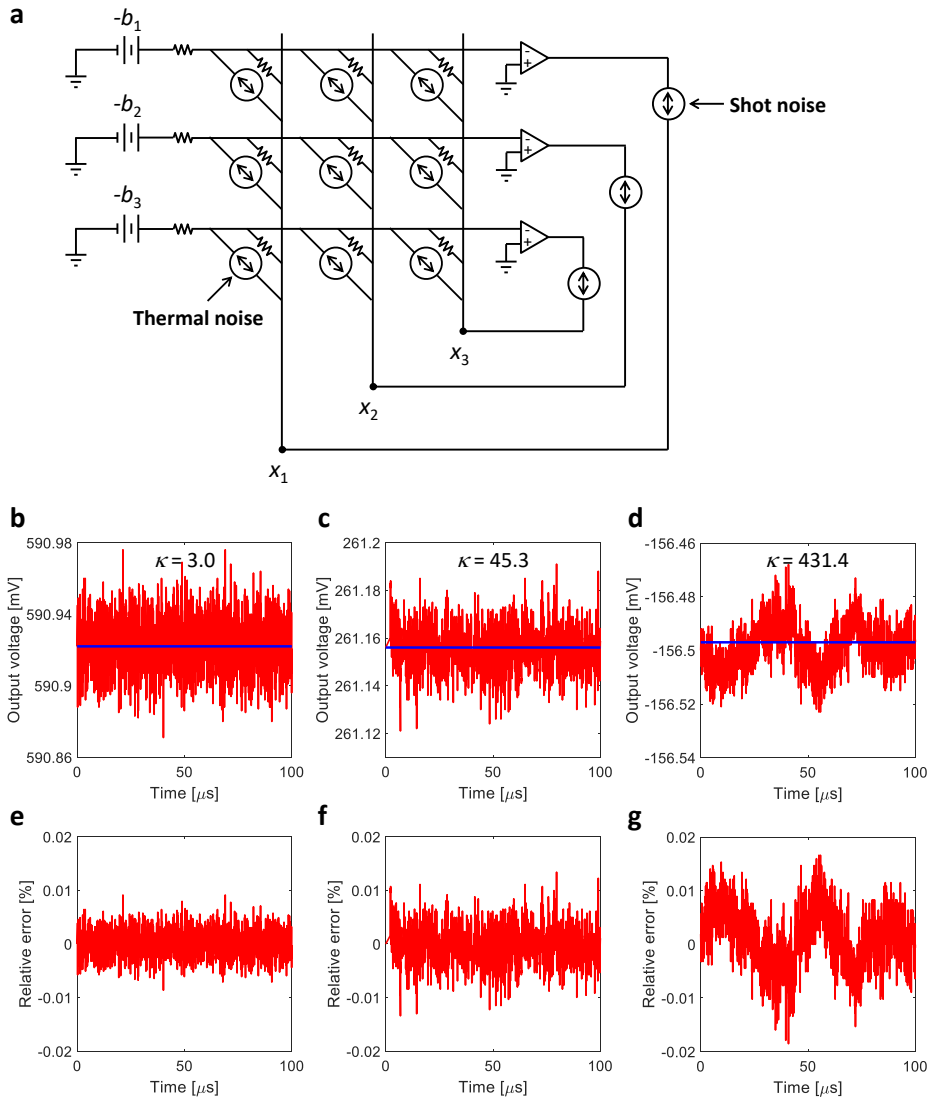
Fig. S15. Condition number dependence of the error caused by device noise. (a) Circuit schematic for noise analysis. Thermal noise and shot noise are included as indicated, referring to (4), which analyzed the noise impact on MVM with a crosspoint array. A typical output voltage for solving a linear system of a matrix with condition number of (b) 3.0, (c) 45.3 and (d) 431.4. Blue lines are output voltages without devise noise, red curves are output voltages with device noise. (e-g) are calculated relative errors based on (b-d), respectively.
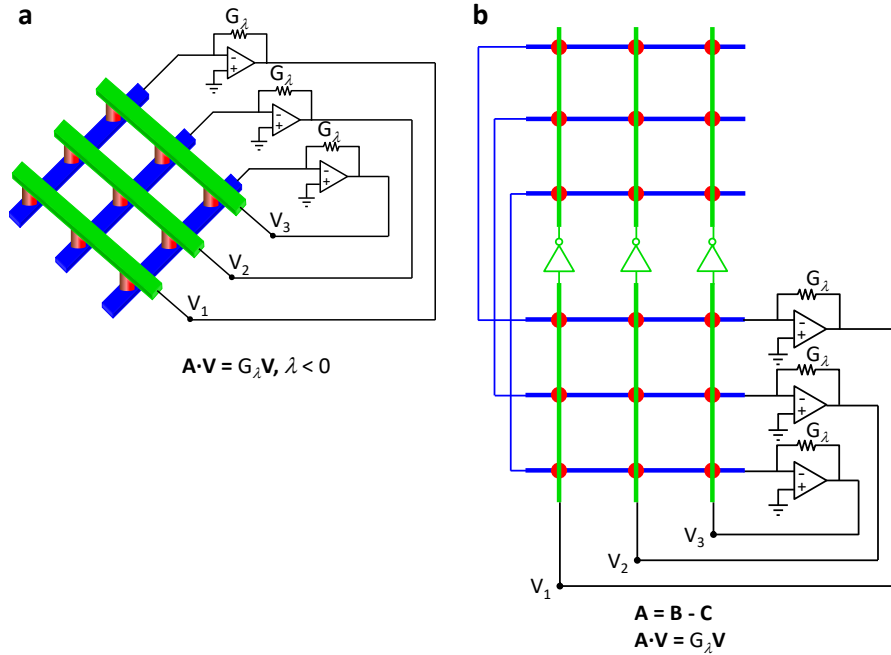
a

$A \cdot V = G_\lambda V, \lambda < 0$

b

$A = B - C$
$A \cdot V = G_\lambda V$

Fig. S16. Eigenvector circuits. (a) Eigenvector circuit for the lowest negative eigenvalue of a positive matrix. The absolute value of negative eigenvalue is mapped into the conductance G_λ of feedback resistors in TIAs. (b) Eigenvector circuit for eigenvalues of a mixed matrix. For negative eigenvalues, the bottom and top crosspoint arrays implement matrix B and C, with $A = B - C$ respectively. On the other hand, for positive eigenvalues, the bottom and top crosspoint arrays implement C and B, respectively. This is because the highest positive eigenvalues of $A = B - C$ is the lowest negative eigenvalue of $-A = C - B$. The absolute values of the eigenvalues are mapped into the conductance G_λ of feedback resistors in TIAs.

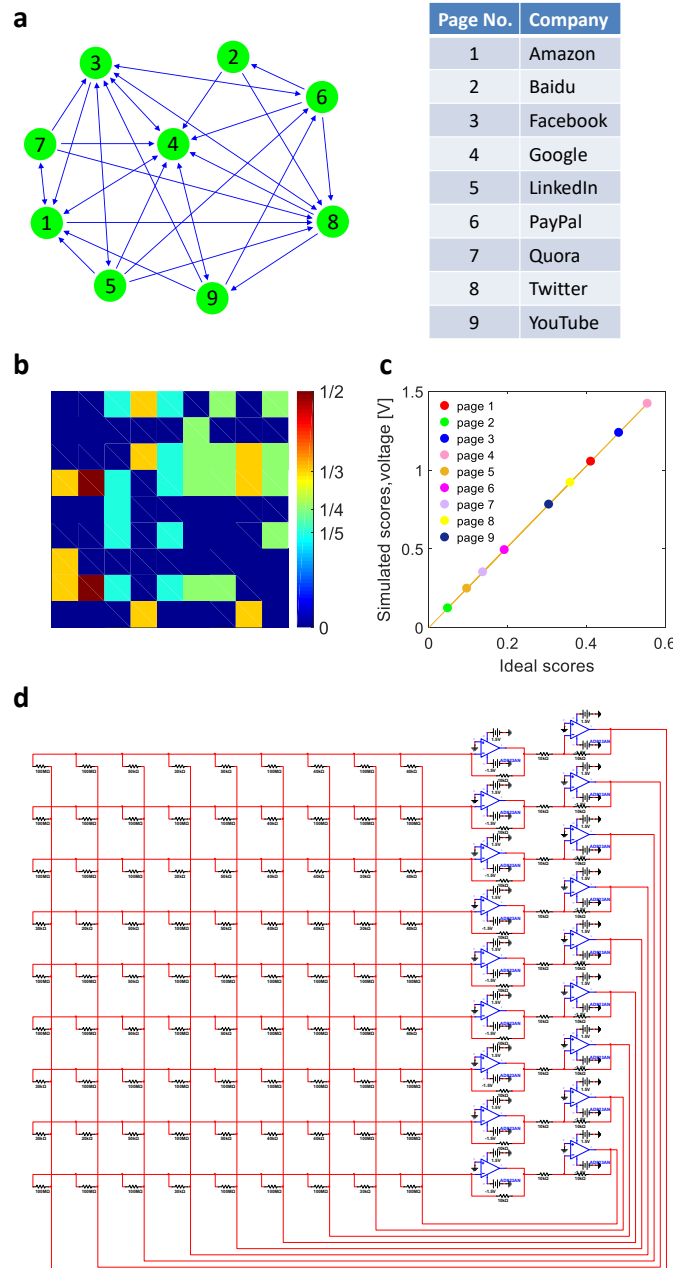| Page No.	Company
1	Amazon
2	Baidu
3	Facebook
4	Google
5	LinkedIn
6	PayPal
7	Quora
8	Twitter
9	YouTube

Fig. S17. A real-world PageRank case. (a) A system of 9 web pages, namely the WikiPedia pages of internet companies indicated in the table on the right. (b) Link matrix of the pages. (c) Calculated importance scores of the pages obtained from a circuit simulation, as a function of the analytically calculated eigenvector. In the circuit simulation, the supply voltage of amplifiers was ± 1.5 V, thus the maximum output voltage was saturated around 1.5 V. The straight line through the coordinate origin indicates the scores are correctly solved. (d) Crosspoint circuit used in the simulation. The transformation unit for conductance is 100 μS, which is also the value of eigenvalue resistors. The zero elements are implemented with high-resistance resistors of 0.01 μS.

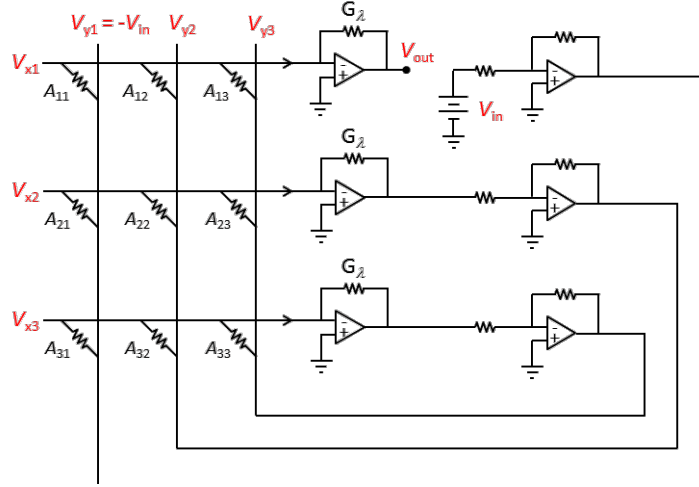**Loop gains of the eigenvector circuit.**

Fig. S18. Calculation of G_{loop} for the eigenvector circuit. In the eigenvector crosspoint circuit, the loop is cut at the output of the first TIA to compute G_{loop1} thus leading to the following six equations:

$$\left(V_{y1}-V_{x1}\right)A_{11}+\left(V_{y2}-V_{x1}\right)A_{12}+\left(V_{y3}-V_{x1}\right)A_{13}=\left(V_{x1}-V_{out}\right)G_{\lambda}, \; V_{out}=-G_{OL}V_{x1},$$

$$\left(V_{y1}-V_{x2}\right)A_{21}+\left(V_{y2}-V_{x2}\right)A_{22}+\left(V_{y3}-V_{x2}\right)A_{23}=\left(V_{x2}+V_{y2}\right)G_{\lambda}, \; V_{y2}=G_{OL}V_{x2},$$

$$\left(V_{y1}-V_{x3}\right)A_{31}+\left(V_{y2}-V_{x3}\right)A_{32}+\left(V_{y3}-V_{x3}\right)A_{33}=\left(V_{x3}+V_{y3}\right)G_{\lambda}, \; V_{y3}=G_{OL}V_{x3},$$

which can be solved to yield the following expression for G_{loop1}:

$$G_{loop1}=\frac{1}{G_{\lambda}+\dfrac{A_1^*}{G_{OL}}}\frac{\begin{vmatrix} A_{11} & A_{12} & A_{13} \\ A_{21} & A_{22}-G_{\lambda}-\dfrac{A_2^*}{G_{OL}} & A_{23} \\ A_{31} & A_{32} & A_{33}-G_{\lambda}-\dfrac{A_3^*}{G_{OL}} \end{vmatrix}}{\begin{vmatrix} A_{22}-G_{\lambda}-\dfrac{A_2^*}{G_{OL}} & A_{23} \\ A_{32} & A_{33}-G_{\lambda}-\dfrac{A_3^*}{G_{OL}} \end{vmatrix}}$$

where $A_1^* = A_{11} + A_{12} + A_{13} + G_{\lambda}$, $A_2^* = A_{21} + A_{22} + A_{23} + G_{\lambda}$, $A_3^* = A_{31} + A_{32} + A_{33} + G_{\lambda}$. and G_{OL} is the open-loop gain of the OAs, assumed equal to 2×10^5 in the simulation. G_{λ} is the conductance corresponding to the highest positive eigenvalue of A. Since G_{OL} is very large, the additional terms in the diagonal elements can be ignored, thus leading to:

$$G_{loop1} = \dfrac{\begin{vmatrix} A_{11}-G_\lambda & A_{12} & A_{13} \\ A_{21} & A_{22}-G_\lambda & A_{23} \\ A_{31} & A_{32} & A_{22}-G_\lambda \end{vmatrix} + G_\lambda \begin{vmatrix} A_{22}-G_\lambda & A_{23} \\ A_{32} & A_{33}-G_\lambda \end{vmatrix}}{G_\lambda \begin{vmatrix} A_{22}-G_\lambda & A_{23} \\ A_{32} & A_{33}-G_\lambda \end{vmatrix}} = \dfrac{G_\lambda \begin{vmatrix} A_{22}-G_\lambda & A_{23} \\ A_{32} & A_{33}-G_\lambda \end{vmatrix}}{G_\lambda \begin{vmatrix} A_{22}-G_\lambda & A_{23} \\ A_{32} & A_{33}-G_\lambda \end{vmatrix}} = 1$$

Similar analysis of the second loop and third loop also lead to similar conclusions, namely:

$$G_{loop2} = \dfrac{G_\lambda \begin{vmatrix} A_{11}-G_\lambda & A_{13} \\ A_{31} & A_{33}-G_\lambda \end{vmatrix}}{G_\lambda \begin{vmatrix} A_{11}-G_\lambda & A_{13} \\ A_{31} & A_{33}-G_\lambda \end{vmatrix}} = 1$$

$$G_{loop3} = \dfrac{G_\lambda \begin{vmatrix} A_{11}-G_\lambda & A_{12} \\ A_{21} & A_{22}-G_\lambda \end{vmatrix}}{G_\lambda \begin{vmatrix} A_{11}-G_\lambda & A_{12} \\ A_{21} & A_{22}-G_\lambda \end{vmatrix}} = 1$$

As a result, if the TIA feedback conductance is chosen equal to the nominal eigenvalue, all G_{loop} are

unit. In practice, the feedback conductance will be slight higher or lower, thus leading to:

$$\begin{vmatrix} A_{11}-G_\lambda & A_{12} & A_{13} \\ A_{21} & A_{22}-G_\lambda & A_{23} \\ A_{31} & A_{32} & A_{22}-G_\lambda \end{vmatrix} \neq 0,$$

As a result, the practical G$_{loop}$ is calculated to be

$$G_{loop1} \approx \dfrac{\begin{vmatrix} A_{11}-G_\lambda & A_{12} \\ A_{21} & A_{22}-G_\lambda \end{vmatrix} + \begin{vmatrix} A_{11}-G_\lambda & A_{13} \\ A_{31} & A_{33}-G_\lambda \end{vmatrix} + \begin{vmatrix} A_{22}-G_\lambda & A_{23} \\ A_{32} & A_{33}-G_\lambda \end{vmatrix}}{\begin{vmatrix} A_{22}-G_\lambda & A_{23} \\ A_{32} & A_{33}-G_\lambda \end{vmatrix}} \dfrac{\Delta G_\lambda}{G_\lambda} + 1$$

where $\Delta G_\lambda = G_\lambda - G_{\lambda,\exp}$ is the error in eigenvalue conductance.

If $\Delta G_\lambda > 0$, then $G_{loop1} > 1$; if $\Delta G_\lambda < 0$, then $G_{loop1} < 1$, which applies to other loop gains. Thus, for G_{loop} to be larger than 1, the eigenvalue conductance should be slightly lower than the nominal value. The same conclusion is obtained for the lowest negative eigenvalue.

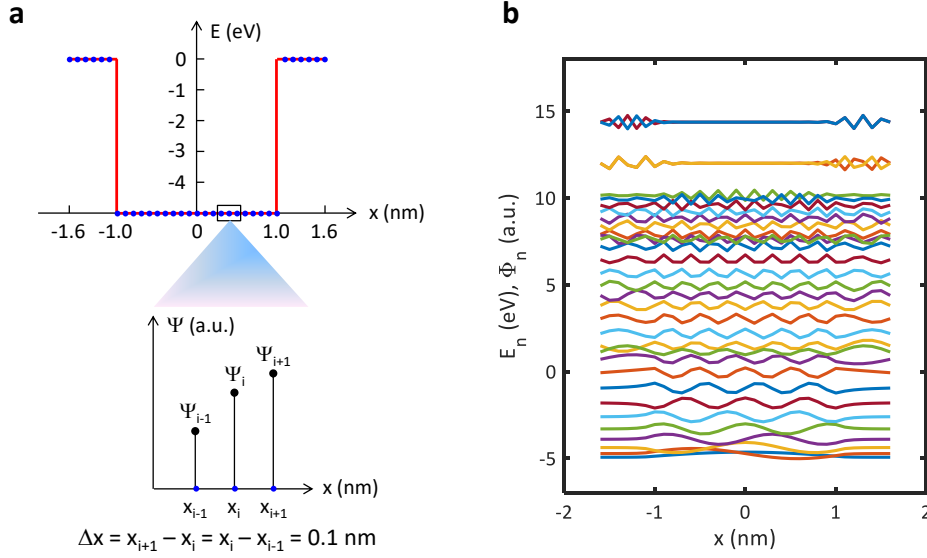## Solving the 1-dimensional time-independent Schrödinger equation.

Fig. S19. Circuit solution of the Schrödinger equation. (a) Potential well and 33 discrete points to discretize the Schrödinger equation with a finite difference method. The distance between two points is 0.1 nm. (b) Energy states (eigenvalues) and normalized wave functions (eigenvectors) for the potential well calculated by MATLAB.

The time-independent Schrödinger equation is given by:

$$\left(-\frac{\hbar^2}{2m}\frac{\partial^2}{\partial x^2} + V(x) \right)\Psi(x) = E\Psi(x)$$

Where $\hbar$ is the reduced Planck constant, $V(x)$ is the potential distribution, Ψ is eigenfunction, and E is the energy eigenvalue. The potential was assumed to have a rectangular shape, with:

$V(x)$ = -5 eV, for -1 $\leqslant x \leqslant$ 1 nm,

$V(x)$ = 0, for -1.6 $\leqslant x <$ -1 nm, and 1 $< x \leqslant$ 1.6 nm.

The Schrödinger equation can be solved numerically by the finite difference method, where the potential well is discretized in 33 points (a), where the first and second derivatives are approximated by the incremental ratios:

$$\frac{d\Psi}{dx} \approx \frac{\Psi_{i+1} - \Psi_i}{\Delta x},$$

$$\frac{d^2\Psi}{dx^2} \approx \frac{\dfrac{\Psi_{i+1} - \Psi_i}{\Delta x} - \dfrac{\Psi_i - \Psi_{i-1}}{\Delta x}}{\Delta x} = \frac{\Psi_{i+1} - 2\Psi_i + \Psi_{i-1}}{\Delta x^2}$$

where Δx = 0.1 nm.

As a result, the Schrödinger equation is transformed into:

$$-\frac{\hbar^2}{2m\Delta x^2}\Psi_{i-1} + \left(\frac{\hbar^2}{m\Delta x^2} + V_i \right)\Psi_i - \frac{\hbar^2}{2m\Delta x^2}\Psi_{i+1} = E\Psi_i,$$

26

with the normalization condition on the square modulus given by:

$$\int_{-\infty}^{\infty} |\Psi(x)|^2 \, dx = 1 ,$$

and the boundary conditions $\Psi_1 = \Psi_N = 0$. The Schrödinger equation is then transformed into a linear system with matrix form:

$$
\begin{bmatrix}
\dfrac{\hbar^2}{m\Delta x^2} + V_1 & 0 & 0 & 0 & \cdots & 0 & 0 \\[2ex]
-\dfrac{\hbar^2}{2m\Delta x^2} & \dfrac{\hbar^2}{m\Delta x^2} + V_2 & -\dfrac{\hbar^2}{2m\Delta x^2} & 0 & \cdots & 0 & 0 \\[2ex]
0 & -\dfrac{\hbar^2}{2m\Delta x^2} & \dfrac{\hbar^2}{m\Delta x^2} + V_3 & -\dfrac{\hbar^2}{2m\Delta x^2} & \cdots & 0 & 0 \\[2ex]
\cdots & \cdots & \cdots & \cdots & \cdots & \cdots & \cdots \\[1ex]
0 & 0 & 0 & 0 & \cdots & -\dfrac{\hbar^2}{2m\Delta x^2} & 0 \\[2ex]
0 & 0 & 0 & 0 & \cdots & \dfrac{\hbar^2}{m\Delta x^2} + V_{N-1} & -\dfrac{\hbar^2}{2m\Delta x^2} \\[2ex]
0 & 0 & 0 & 0 & \cdots & 0 & \dfrac{\hbar^2}{m\Delta x^2} + V_N
\end{bmatrix}
\begin{bmatrix}
\Psi_1 \\ \Psi_2 \\ \Psi_3 \\ \cdots \\ \Psi_{N-2} \\ \Psi_{N-1} \\ \Psi_N
\end{bmatrix}
= E
\begin{bmatrix}
\Psi_1 \\ \Psi_2 \\ \Psi_3 \\ \cdots \\ \Psi_{N-2} \\ \Psi_{N-1} \\ \Psi_N
\end{bmatrix}
$$

where the matrix eigenvalues correspond to energy eigenvalues, while matrix eigenvectors correspond to the discretized eigenfunction (Fig. S19b).

For the eigenvector circuit, if the lowest negative eigenvalue (ground state energy) is known, the eigenvector (wave function) can be computed directly.
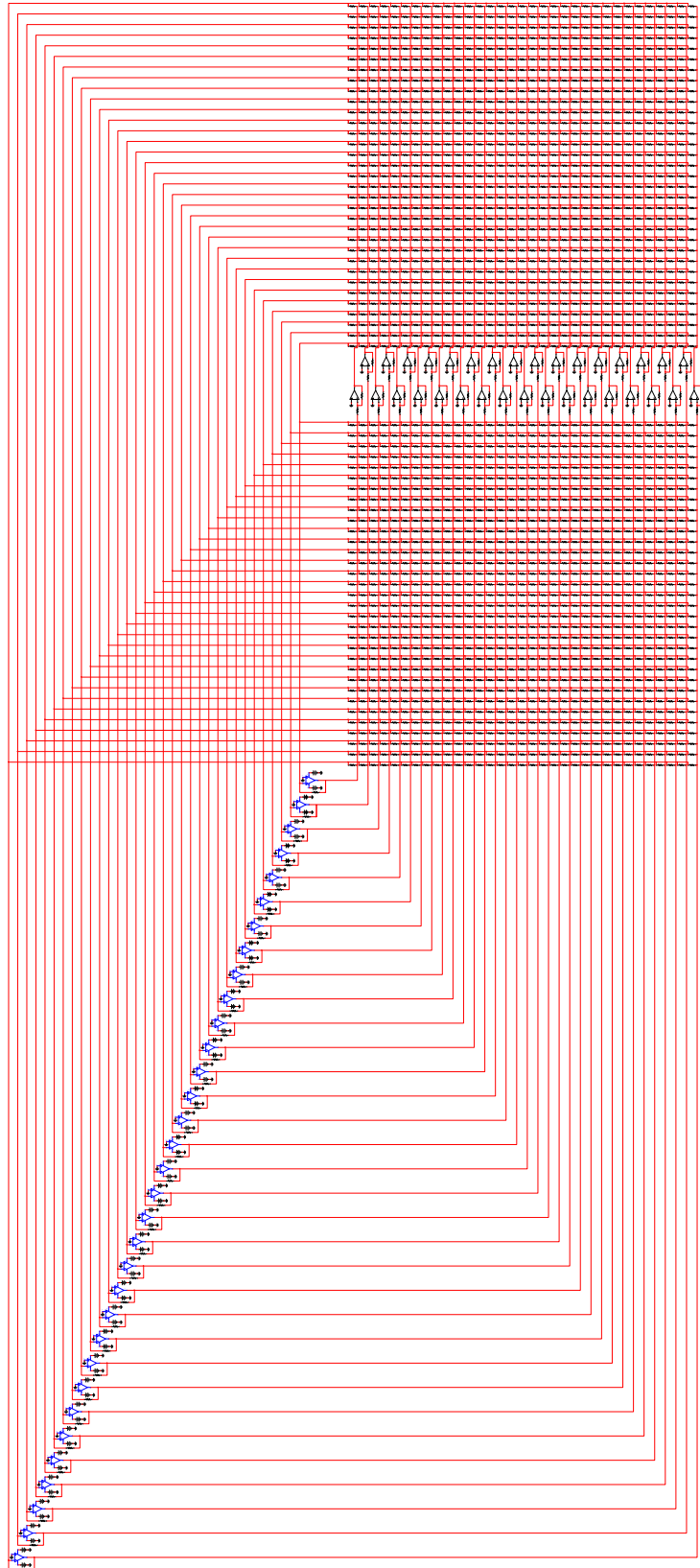
The simulation circuit is shown in Fig. S20.

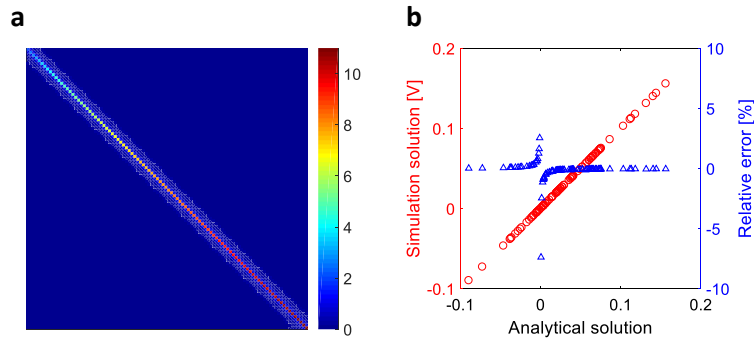**Fig. S20. Simulation circuit for solving the Schrödinger equation.**

Fig. S21. Solving a linear system of a model covariance matrix, whose size is 100×100. (a) A covariance matrix A is defined as $A_{ij} = 1 + \sqrt{i}$, if $i = j$, otherwise $A_{ij} = \frac{1}{|i-j|}$. The condition number of matrix A is 15.5. (b) Simulation results for solving a linear system $Ax = b$, where the matrix A was mapped to a crosspoint resistive array, the entries of b were generated uniformly in [0, 1], and the circuit was simulated in LTspice to give the solution. The calculated relative errors are plotted as the right y-axis. The extremely low solution errors demonstrate the feasibility of the circuit for solving large-scale problems.
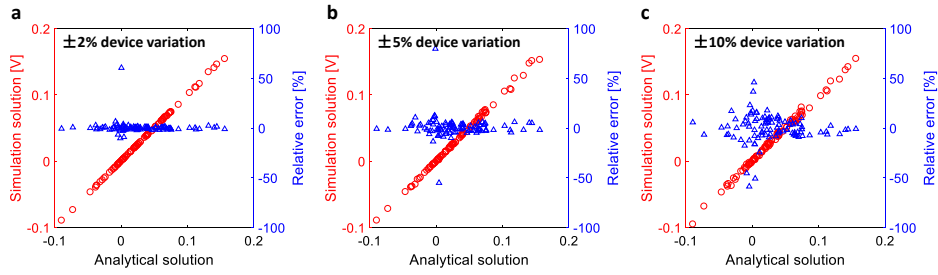
Fig. S22. Impact of device variations on the circuit solution of a linear system of equations. (a) Simulation results for the solution of the linear system of Fig. S21, assuming a random variation within $\pm 2\%$ for the conductance of each memory device with respect to the ideal value. (b) Same as (a), but the random errors are within $\pm 5\%$. (c) Same as (a), but the random errors are within $\pm 10\%$. The calculated relative errors are plotted as the right *y*-axis in each plot. Random errors within a certain range are assumed to follow a uniform distribution.
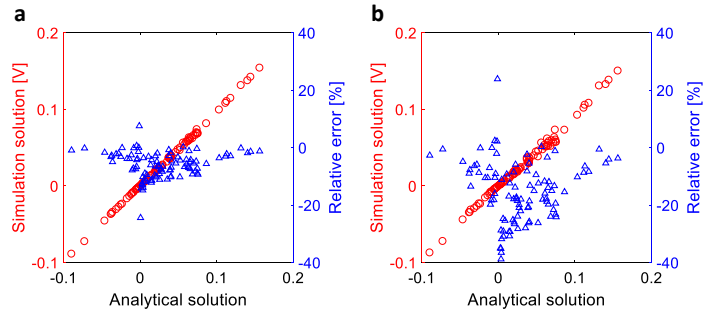
Fig. S23. Impact of the parasitic resistance on the circuit solution of a linear system of equations.
(a) Correlation plot of the circuit solution as a function of the ideal analytical solution for the linear system with the 100×100 covariance matrix of Fig. S21. The wire parasitic resistance R_W between adjacent memory elements was assumed to be $R_W = 1$ Ω, corresponding to the 65 nm technology node. The relative errors are also shown (see the right *y*-axis). (b) Same as (a), but for $R_W = 3$ Ω corresponding to the 22 nm node.

References

1. Lee HY, et al. (2008) Low Power and High Speed Bipolar Switching with A Thin Reactive Ti Buffer Layer in Robust HfO_2 Based RRAM. *IEDM Tech Dig*, pp 1-4.
2. Ielmini D (2011) Modeling the universal set/reset characteristics of bipolar RRAM by field- and temperature-driven filament growth. *IEEE Trans Electron Devices* 58:4309-4317.
3. Ambrogio S, Balatti S, Gilmer DC, Ielmini D (2014) Analytical modeling of oxide-based bipolar resistive memories and complementary resistive switches. *IEEE Trans Electron Devices* 61:2378-2386.
4. Hu M, et al. (2016) Dot-product engine for neuromorphic computing: programming 1T1M crossbar to accelerate matrix-vector multiplication. in *2016 53nd ACM/EDAC/IEEE Design Automation Conference (DAC)*, pp 1-6.